J. Fluid Mech. (2019), *vol.* 867, *pp.* 556–571. © Cambridge University Press 2019
doi:10.1017/jfm.2019.161

Capillary waves control the ejection of bubble bursting jets

J. M. Gordillo[1,†] **and J. Rodríguez-Rodríguez**[2]

[1]Grupo de Mecánica de Fluidos, Departamento de Ingeniería Aeroespacial y Mecánica de Fluidos, Universidad de Sevilla, Avenida de los Descubrimientos s/n 41092, Sevilla, Spain

[2]Grupo de Mecánica de Fluidos, Universidad Carlos III de Madrid, 28911, Leganés, Spain

(Received 27 November 2018; revised 29 January 2019; accepted 17 February 2019; first published online 25 March 2019)

Here we provide a theoretical framework describing the generation of the fast jet ejected vertically out of a liquid when a bubble, resting on a liquid–gas interface, bursts. The self-consistent physical mechanism presented here explains the emergence of the liquid jet as a consequence of the collapse of the gas cavity driven by the low capillary pressures that appear suddenly around its base when the cap, the thin film separating the bubble from the ambient gas, pinches. The resulting pressure gradient deforms the bubble which, at the moment of jet ejection, adopts the shape of a truncated cone. The dynamics near the lower base of the cone, and thus the jet ejection process, is determined by the wavelength λ^* of the smallest capillary wave created during the coalescence of the bubble with the atmosphere which is not attenuated by viscosity. The minimum radius at the lower base of the cone decreases, and hence the capillary suction and the associated radial velocities increase, with the wavelength λ^*. We show that λ^* increases with viscosity as $\lambda^* \propto Oh^{1/2}$ for $Oh \lesssim O(0.01)$, with $Oh = \mu/\sqrt{\rho R \sigma}$ the Ohnesorge number, R the bubble radius and ρ, μ and σ indicating respectively the liquid density, viscosity and interfacial tension coefficient. The velocity of the extremely fast and thin jet can be calculated as the flow generated by a continuous line of sinks extending along the axis of symmetry a distance proportional to λ^*. We find that the jet velocity increases with the Ohnesorge number and reaches a maximum for $Oh = Oh_c$, the value for which the crest of the capillary wave reaches the vertex of the cone, and which depends on the Bond number $Bo = \rho g R^2/\sigma$. For $Oh > Oh_c$, the jet is ejected after a bubble is pinched off; in this regime, viscosity delays the formation of the jet, which is thereafter emitted at a velocity which is inversely proportional to the liquid viscosity.

Key words: aerosols/atomization, breakup/coalescence, bubble dynamics

1. Introduction

The description of the physical mechanisms governing the ejection of drops from bubbles laying on a liquid–gas interface has been the subject of recent research efforts for its implication in many natural and industrial processes as diverse as climate (MacIntyre 1972; Veron 2015), the dispersion of contaminants (Walls, Bird & Bourouiba 2014) or the wine industry (Ghabache *et al.* 2016). Indeed, the bursting of

† Email address for correspondence: jgordill@us.es

https://doi.org/10.1017/jfm.2019.161 Published online by Cambridge University Press

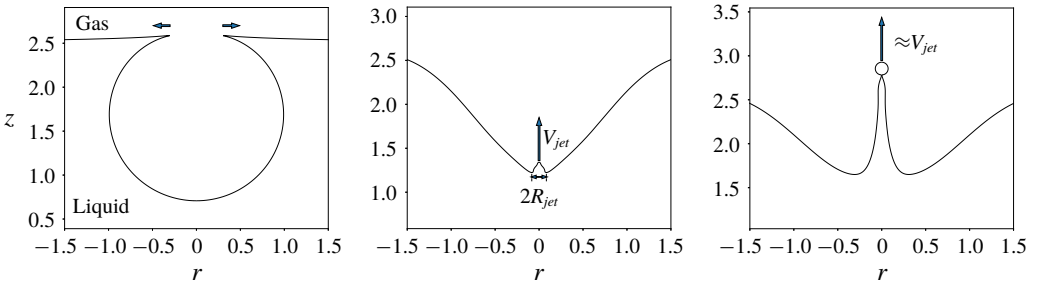


FIGURE 1. (Colour online) Sketch showing the sequence of events following the bursting of a bubble resting initially on a free interface. The retraction of the rim causes a convergent flow towards the base of the cavity that favours the formation of a fast jet of initial velocity V_{jet} and initial radius R_{jet}. The formation of a long liquid jet is the signature that the Weber number verifies the condition, $\rho V_{jet}^2 R_{jet}/\sigma \gg 1$, which implies that the tip of the jet is not appreciably decelerated by capillarity.

the type of bubbles generated by breaking waves in the ocean, whitecaps, produces a sea spray composed by drops which, after evaporation, is responsible for the emission into the atmosphere of micron and submicron-sized particles composed by salt, sulphates or even organic compounds (Bigg & Leck 2008). It is well known that these particles act as condensation nuclei for rain and also contribute to the albedo effect, either directly, or favouring the formation of clouds which reflect the incident sunlight (de Leeuw *et al.* 2011). Drops are produced in bubble bursting events as a consequence of the rupture of either the bubble cap (cap drops) (Spiel 1998; Lhuissier & Villermaux 2012) or of the Worthington-like jet (Worthington & Cole 1896) created after cavity collapse (jet drops) (MacIntyre 1972; Duchemin *et al.* 2002; Walls, Henaux & Bird 2015; Ghabache & Seon 2016).

In this contribution we focus on the description of the physical processes governing the production of the violent Worthington jets ejected when a bubble, initially at rest at an interface, bursts – see figure 1. The sequence of events following the breakup of the liquid film separating the bubble from the atmosphere reveals that, as soon as a hole is nucleated at the bubble surface, capillarity widens the initial orifice, generating capillary waves propagating along the bubble interface (MacIntyre 1972; Duchemin *et al.* 2002; Ghabache *et al.* 2014; Krishnan, Hopfinger & Puthenveettil 2017). Once these waves reach the base of the bubble, a high-speed Worthington jet is ejected vertically upwards and, usually, tiny droplets with diameters noticeably smaller than that of the bubbles from which they are produced, are issued from the tip of the highly stretched jet. Such micrometre-sized droplets are present in our daily life experience: indeed, they are felt at the instant they impact against our face when drinking a soda or another type of carbonated drink and are also perceived indirectly, through the aroma, which is enhanced thanks to mass transfer from the drop to the atmosphere (Ghabache *et al.* 2016).

Interestingly, the velocities of bubble bursting drops exceed, by far, the capillary velocity. Indeed, consider a bubble of radius R immersed in a liquid of density ρ, viscosity μ and interfacial tension coefficient σ such that the Bond number verifies the condition $Bo = \rho g R^2/\sigma \ll 1$. For bubbles with radii $R = 3 \times 10^{-4}$ m in water ($\rho = 1000$ kg m^{-3}, $\mu = 10^{-3}$ Pa s and $\sigma = 0.072$ N m^{-1}) $Bo \simeq 0.01 \ll 1$ and the velocity of the first drops ejected is $\simeq 10$ m s^{-1} (Ghabache *et al.* 2014), namely, twenty times the capillary velocity $\sqrt{\sigma/(\rho R)} \simeq 0.5$ m s^{-1}. This striking result, together

https://doi.org/10.1017/jfm.2019.161 Published online by Cambridge University Press

with the additional finding in Ghabache *et al.* (2014) that the velocities of the drop produced could be fitted by a power law of the type $\propto R^{-1}$, permits us to conclude that the scaling for the jet velocity proposed in the seminal work by Duchemin *et al.* (2002), $\sqrt{\sigma/(\rho R)} \propto R^{-1/2}$, cannot be valid along the whole range of values of the only dimensionless parameter characterizing the bursting of bubbles in the limit $Bo \to 0$ namely, the Ohnesorge number, $Oh = \mu/\sqrt{\rho R \sigma}$. Another relevant finding in Duchemin *et al.* (2002) and Ghabache *et al.* (2014) is that, for a given bubble radius, the velocities of the droplets ejected increase with μ for liquid viscosities below $\sim$10 times that of water. Not surprisingly, the same group of authors found that the jet velocity decreases for larger values of μ. Thus, the results in Duchemin *et al.* (2002) and Ghabache *et al.* (2014) indicate that, for a given value of $Bo \ll 1$, there exists a range of values of the Ohnesorge number for which the bursting of bubbles in more viscous liquids produces faster jets. Another interesting result, reported by Walls *et al.* (2015), is that the main effect of the Bond number on the jet ejection process does not come through the deceleration of the vertical liquid column but from the initial shape of the bubble, which is uniquely determined by the value of Bo. Walls *et al.* (2015) also reported that the jet and drop ejection processes are favoured by low values of Bo, for which bubbles are spherical and the minimum depth of the cavity is located at a distance from the unperturbed free interface of, approximately, two times the bubble radius.

In two recent contributions Gañán Calvo (2017, 2018) provides scalings for both the velocities and diameters of the first jet drops produced after bubble bursting that agree fairly well with a set of experimental and numerical results reported in the literature. However, as explained in Gordillo & Rodríguez-Rodríguez (2018), this model rests on hypotheses that yield other predictions which are inconsistent with numerical results. Moreover, as will be explained below, when extended to a wider range of conditions, the model exhibits singularities that are not consistent with observations. The reason behind these inconsistencies is that at the heart of the model is the assumption that the high-speed jet emerges as a consequence of viscous shear stress. Indeed, the equation for the jet velocity in Gañán Calvo (2017) reads, using our variables,

$$V_{jet} \simeq 16\frac{\sigma}{\mu}[Oh^{-2}(Oh^* - Oh)]^{-3/4} = 16\sqrt{\sigma/(\rho R)}Oh^{1/2}(Oh^* - Oh)^{-3/4}, \tag{1.1}$$

with $Oh^* \simeq 0.043$. Notice that our variables R and V_{jet} in (1.1) are used to denote the initial bubble radius and the initial jet velocity, but these quantities are termed in Gañán Calvo (2017, 2018) R_0 and V respectively because R in Gañán Calvo (2017, 2018) denotes the jet radius at the ejection instant while we represent this variable here as R_{jet} (see figure 1). Moreover, L indicates in Gañán Calvo (2017, 2018) an arbitrary wavelength, a quantity which is termed here using $\Lambda = \lambda R$, with λ the corresponding dimensionless wavelength. Equation (1.1) was deduced in Gañán Calvo (2017) making use, among others, of momentum and mass balances which, using our variables, read

$$\rho V_{jet}^2 \sim \mu\frac{V_\Lambda}{\Lambda}, \quad V_{jet}R_{jet}^2 \sim V_\Lambda \Lambda R_{jet}, \tag{1.2a,b}$$

with $V_\Lambda = \sqrt{\sigma/(\rho\Lambda)}$ the capillary velocity corresponding to the wavelength Λ (Gañán Calvo 2018). The low Ohnesorge limit of (1.1), which expresses that

$$V_{jet} \propto \sqrt{\sigma/(\rho R)}Oh^{1/2}, \tag{1.3}$$

https://doi.org/10.1017/jfm.2019.161 Published online by Cambridge University Press

combined with $V_\Lambda \propto \sqrt{\sigma/(\rho\Lambda)}$ and the momentum balance in (1.2) yields $\Lambda \propto R$ and $V_\Lambda \propto \sqrt{\sigma/(\rho R)}$. Hence, the balances in (1.2) express that, in the low Ohnesorge limit, viscosity sets in motion a region of width of the order of the radius of the bubble beneath the propagating wave and that the viscous shear stress accelerates the liquid beneath the bubble into a thin, fast jet. Indeed, notice that the physical argument provided in Gañán Calvo (2017) to recover the experimental trend expressed by (1.3) in the limit $Oh \ll 1$ – see (1.2) – is:

$$\rho V_{jet}^2 \sim \mu \frac{\sqrt{\sigma/(\rho R)}}{R}, \quad V_{jet} R_{jet}^2 \sim R_{jet} R \sqrt{\sigma/(\rho R)}. \tag{1.4a,b}$$

But this conclusion is in contradiction with boundary layer theory, from which it is well known that the thickness of the region affected by viscosity beneath a shear-free interface is $\sqrt{\nu T_r}$, with $\nu = \mu/\rho$ the kinematic viscosity and $T_r \sim \Lambda/V_\Lambda$ the residence time (Moore 1963). Indeed, since the theory in Gañán Calvo (2017, 2018) predicts that $\Lambda \propto R$ and $V_\Lambda \propto \sqrt{\sigma/(\rho R)}$ for $Oh \ll 1$, the boundary layer thickness corresponding to this limit is

$$\sqrt{\frac{\mu}{\rho}\left(\frac{\rho R^3}{\sigma}\right)^{1/2}} \propto R Oh^{1/2} \ll \Lambda \sim R, \tag{1.5}$$

namely, the thickness of the region beneath the bubble which is affected by viscosity is much smaller than the initial bubble radius, a fact confirmed by the vorticity contours depicted in the numerical simulations of the next section and in Gordillo & Rodríguez-Rodríguez (2018). To further support our claims, notice that a necessary condition for a long liquid jet to be formed in any physical context involving low viscosity liquids (low values of the Ohnesorge number) is that the momentum flux feeding the jet overcomes the capillary forces, i.e. $\rho V_{jet}^2 R_{jet}/\sigma \gtrsim O(1)$ (Eggers & Villermaux 2008), see figure 1. However, making use of the first equation in (1.4), the theory in Gañán Calvo (2017, 2018) predicts that, in contrast with experimental evidence, a long jet cannot be generated because

$$\frac{\rho V_{jet}^2 R_{jet}}{\sigma} < \frac{\rho V_{jet}^2 R}{\sigma} \sim Oh \ll 1. \tag{1.6}$$

It is the purpose of this contribution to present a theoretical framework that describes the formation of the high-speed Worthington jet ejected after bubble bursting. Our theory extends to all of the range of Ohnesorge numbers where a droplet is ejected, in particular describing well the region of maximum jet speed, while recovering the limit of low Ohnesorge number already described in the literature. We show that the dynamics of the jet is not driven by viscosity but by a purely inertial mechanism which is modulated by viscosity through the selection of the wavelength of the capillary waves excited during the rim retraction process. Our inertial theory not only recovers the low Ohnesorge limit expressed by (1.3), which reproduces experimental and numerical results, but also explains the abrupt decrease in jet velocity reported by Duchemin *et al.* (2002) and Deike *et al.* (2018) above a certain value of the Ohnesorge number, a result that contrasts with the prediction in Gañán Calvo (2017) that jet velocity diverges as Oh approaches $Oh^* \simeq 0.043$, see (1.1).

The paper is structured as follows: § 2 is dedicated to scaling the wavelength of the capillary wave selected during the rim retraction process, § 3 is devoted to presenting a theory linking the jet ejection velocity with the wavelength of the selected capillary wave travelling towards the bottom of the collapsing cavity and the main ideas are summarized in § 4.

https://doi.org/10.1017/jfm.2019.161 Published online by Cambridge University Press

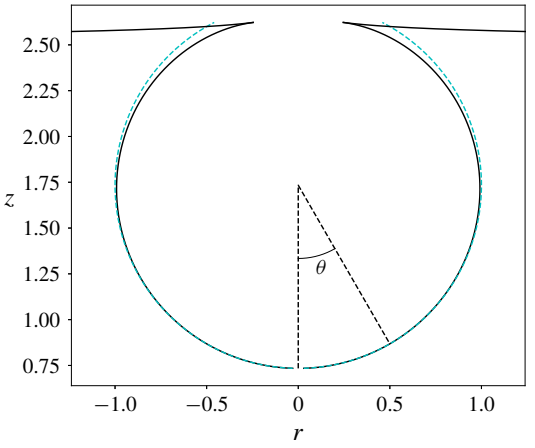


FIGURE 2. (Colour online) Shape of the bubble at $t=0$. The black thick lines correspond to the numerical solution of the hydrostatic equations describing a bubble resting on a free surface as described in Lhuissier & Villermaux (2012). The cyan dashed line corresponds to a sphere with a radius equal to that of the bubble at the apex. The figure also defines the angle θ used to characterize the propagation speed of the capillary waves.

2. Wavelength selection during the rim retraction process

In this contribution we will limit ourselves to describing the ejection of Worthington jets from the bursting of bubbles with characteristic radii well below the capillary length. We will perform numerical simulations fixing the value of the Bond number and, therefore, the results obtained will depend on just one dimensionless parameter, namely, the Ohnesorge number, $Oh=\mu/\sqrt{\rho R\sigma}$. In the text, dimensionless variables will be written using lower case letters to differentiate them from their dimensional counterparts (in capital letters). Distances, times and pressures will be made non-dimensional using as characteristic values, R, $\sqrt{\rho R^3/\sigma}$ and σ/R; hence, velocities will be made non-dimensional using as the characteristic value the capillary velocity $\sqrt{\sigma/(\rho R)}$.

Axisymmetric simulations have been performed using the open-source code Gerris (Popinet 2003; Deike *et al.* 2018) using as values for the density and viscosity ratios 1.2×10^{-3} and 1.8×10^{-2} respectively, corresponding to air bubbles in water. The computations are started by suddenly removing the cap of a bubble resting statically on a free surface. The initial shape of the bubble, see figure 2, is found solving the Young–Laplace equation for a constant value of the Bond number, $Bo=\rho g R^2/\sigma=0.05$, which is sufficiently small so that the influence of gravity in the jet ejection process comes only through the initial shape of the bubble (Walls *et al.* 2015). Simulations with different grid refinements have been carried out to check that the results presented here are independent of the numerical grid. The script used to determine the initial shape is provided in the supplementary material available at https://doi.org/10.1017/jfm.2019.161, along with the Gerris code used to perform the simulations.

Capillary waves are excited during the capillary retraction of the liquid film that separates the bubble from the atmosphere, see figure 3 (MacIntyre 1972; Duchemin *et al.* 2002). The description of the ejection of the Worthington jet depicted in the last panel in figure 3 requires us, as a first step, to deduce the value of the dimensionless

https://doi.org/10.1017/jfm.2019.161 Published online by Cambridge University Press

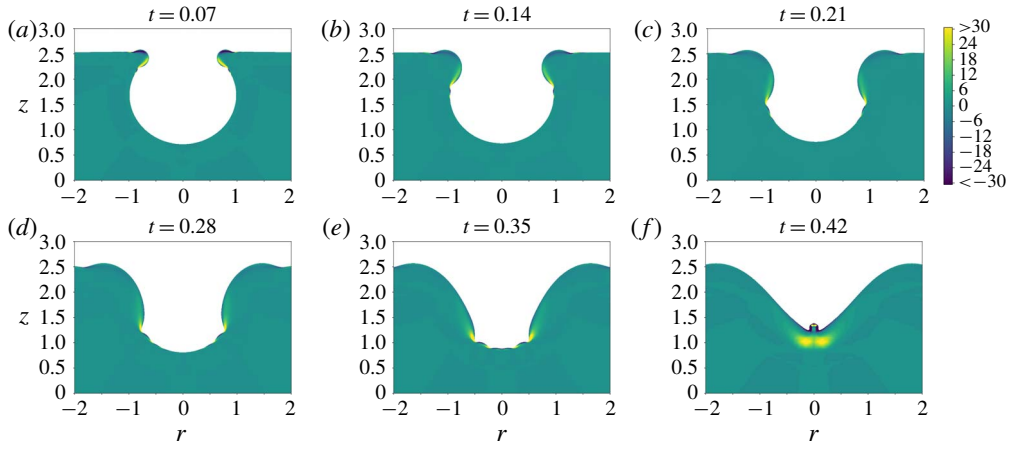


FIGURE 3. (Colour online) Shape of the collapsing cavity and contours of azimuthal vorticity at different instants of time for $Bo = 0.05$ and $Oh = 0.012$. The colour code in the figure indicates the value of the azimuthal vorticity in the liquid. See also the videos included as supplementary material.

length scale λ^* of the waves reaching the bottom of the cavity. (Please note that the selected wavelength λ^* must not be mistaken with λ, which denotes arbitrary values of the dimensionless wavelength.) It is known that the rim retraction excites capillary waves of wavelength proportional to the local thickness of the liquid film located upstream of the blob where the liquid is collected (Taylor 1959; Song & Tryggvason 1999). Hence, it could be thought that the dimensionless wavelength, λ^*, characterizing the first capillary wave reaching the bottom of the cavity, is proportional to the minimum thickness of the liquid film. However, the capillary waves with the smallest wavelengths are rapidly attenuated by viscosity. Consequently, the capillary wave preceding the liquid blob depicted in figure 3 is the one with the shortest wavelength, λ^*, which is not attenuated by viscosity during the time interval characterizing the rim retraction process.

Figure 4 shows that, after a hole is nucleated at the film, a wave of characteristic wavelength λ^*, which increases with Oh, propagates towards the bottom of the cavity at a constant angular velocity which is independent of the Ohnesorge number, a fact that was already noticed by Krishnan *et al.* (2017). Therefore, the time characterizing the rim retraction process is nothing but the capillary time $(\rho R^3/\sigma)^{1/2}$ and hence, the criterion that determines the wavelength of the wave depicted in figure 3 which propagates towards the base of the cavity can be written as

$$\frac{1}{T(\lambda^*)}\left(\frac{\rho R^3}{\sigma}\right)^{1/2} \simeq 1, \tag{2.1}$$

with $1/T(\lambda)$ the viscous attenuation rate, which increases with decreasing values of the dimensionless wavelength λ, as we will show next. Indeed, since the amplitude of capillary waves decreases exponentially in time as $\mathrm{e}^{-t/T}$ (Batchelor 1967), and the time taken by capillary waves to reach the bottom of the cavity is the capillary time, see figure 4, the amplitude of the waves verifying the condition $(\rho R^3/\sigma)^{1/2} \gtrsim T(\lambda)$ will be negligible when they reach the base of the bubble. Hence, the waves with the

https://doi.org/10.1017/jfm.2019.161 Published online by Cambridge University Press

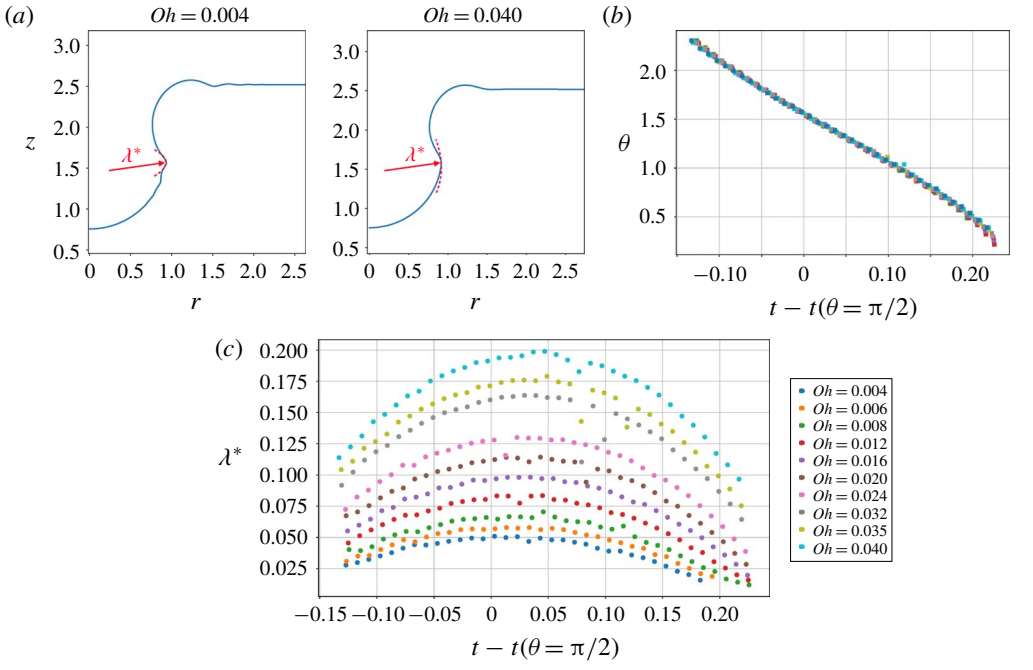


FIGURE 4. (Colour online) (*a*) A wave of characteristic dimensionless wavelength λ^* propagates along the cavity. The wavelength of the capillary wave measured at $\theta = \pi/2$ increases with *Oh*. (*b*) The selected waves propagate at a constant velocity $\simeq 5 \times \sqrt{\sigma/(\rho R)}$, which does not depend on the Ohnesorge number. The origin of time, $t = 0$, is fixed at the instant the bubble bursts. (*c*) Time evolution of the wavelength λ^* corresponding to the wave selected by viscosity for several values of the Ohnesorge number.

shortest wavelengths that will reach the base of the cavity will be those verifying the condition expressed by (2.1) and these waves will control the jet ejection process as we will show in what follows.

Two different scenarios must be considered for the calculation of the attenuation rate, depending on the ratio between the wavelength of a capillary wave excited during rim retraction, λR, and the thickness of the boundary layer that develops around its crest, δR (see the vorticity fields in figure 3). This boundary layer appears to enforce the condition of zero shear stress on a surface with curvature, and it is entirely analogous to that developing around a translating spherical bubble, studied by Moore (1963). Making use of Moore's results, the boundary layer thickness induced by one of the capillary waves excited during the first instants of the rim retraction process is $\sqrt{\nu T_c}$, with T_c the residence time of fluid particles over a wave of wavelength $R\lambda$,

$$\delta R \propto \sqrt{\nu \left(\frac{\rho R^3 \lambda^3}{\sigma} \right)^{1/2}}. \tag{2.2}$$

If $\delta \ll \lambda$, the dissipation of kinetic energy will take place in a spatial region surrounding the wave where the flow is irrotational but, if $\delta \sim \lambda$, the kinetic energy will be dissipated within the boundary layer developing around the wave. The balance of kinetic energy in the region where energy is dissipated yields two

https://doi.org/10.1017/jfm.2019.161 Published online by Cambridge University Press

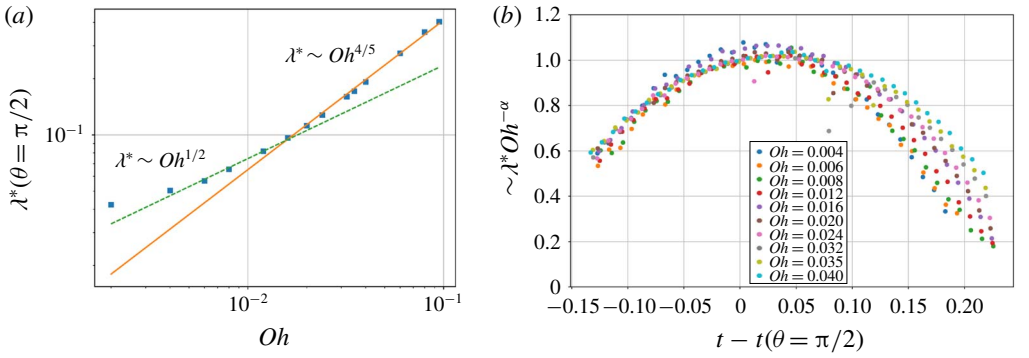


FIGURE 5. (Colour online) (*a*) The wavelength of the selected capillary wave scales as $Oh^{1/2}$ for $Oh \lesssim 0.02$ and as $\propto Oh^{4/5}$ for $Oh \gtrsim 0.02$. (*b*) Time evolution of the wavelengths of the waves excited during rim retraction. These evolutions, depicted in figure 4(*c*), collapse onto a single curve when rescaled with the fits shown in (*a*). Here, $\alpha = 1/2$ for $Oh \leqslant 0.02$ and $\alpha = 4/5$ for $Oh > 0.02$.

different expressions for $1/T$: for the irrotational flow case, $\delta/\lambda \ll 1$, the attenuation rate is given by the well known result in Batchelor (1967) (see also appendix A),

$$\frac{1}{T} \propto \frac{\mu}{\rho R^2 \lambda^2}, \tag{2.3}$$

but, when $\delta \sim \lambda$, the dissipation of kinetic energy takes place within the boundary layer of thickness δ, where the flow is no longer irrotational. In this latter case, the expression for the attenuation rate is (see appendix A for details),

$$\frac{1}{T} \propto \frac{\mu}{\rho R^2} Oh \lambda^{-5/2}. \tag{2.4}$$

Introducing (2.3)–(2.4) into the condition expressed by (2.1), we obtain the following scalings for the wavelength λ^* selected by viscosity during the rim retraction process:

$$\text{If} \quad \lambda \ll \delta : \frac{\mu}{\rho R^2 \lambda^{*2}} \times \left(\frac{\rho R^3}{\sigma}\right)^{1/2} \simeq 1 \Rightarrow \lambda^* \propto Oh^{1/2}. \tag{2.5}$$

$$\text{If} \quad \lambda \sim \delta : \frac{\mu}{\rho R^2} Oh (\lambda^*)^{-5/2} \times \left(\frac{\rho R^3}{\sigma}\right)^{1/2} \simeq 1 \Rightarrow \lambda^* \propto Oh^{4/5}. \tag{2.6}$$

The results in (2.6) are confirmed in figure 5, where it is also depicted that the transition between the two scalings provided in (2.5)–(2.6) takes place for a value of the Ohnesorge number $Oh \sim 0.02$. The numerical value of λ^* corresponding to $Oh = 2 \times 10^{-3}$ in figure 5 slightly deviates from $\lambda^* \propto Oh^{1/2}$, this fact being associated with how the selected wavelength represented in figure 4 is measured numerically, as is supported by the fact that it does not have any consequence in the scaling of the jet velocity, as we will show in what follows. Remarkably, figure 5 confirms the robustness of each of the scalings in (2.6), which are valid in approximately one decade in Oh, namely, in two decades of the Laplace number, defined as $La = Oh^{-2}$, which is the dimensionless number used in other references (Deike *et al.* 2018; Lai, Eggers & Deike 2018).

https://doi.org/10.1017/jfm.2019.161 Published online by Cambridge University Press

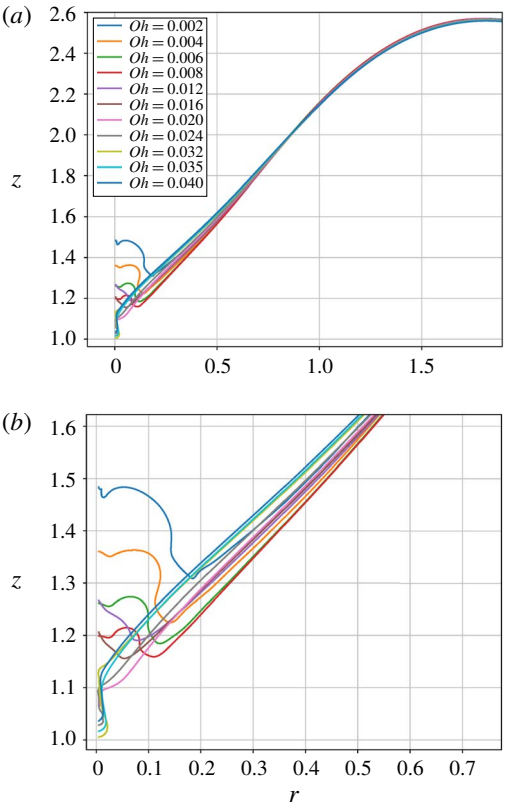


FIGURE 6. (Colour online) (*a*) The shape of the collapsing cavity at the instant of jet ejection can be approximated by a truncated cone for $Oh < Oh_c$. For $Oh > Oh_c$, the crest of the waves reaches the vertex and a tiny bubble is entrapped below the collapsing cavity. (*b*) Zoom of the base of the collapsing cavity, from which the jet is issued, which can be approximated by a truncated cone, see the sketch in figure 7. Notice that, for the value of the Bond number considered here, $Bo = 0.05$, bubbles are entrapped for $Oh \gtrsim 0.02$. From that value onwards, the range of values for which a satellite bubble is formed, the jet velocity decreases, see figure 8(*a*). The bubble is entrapped as a consequence of the fact that the amplitude of the wave excited during the rim retraction process is such that the minimum height of this wave is below the vertex of the cone. Observe in this figure and in figure 8(*a*) that the maximum jet velocity is attained for the value of the Ohnesorge number for which the bottom part of the wave reaches the vertex of the truncated cone.

Let us point out that, by including the dissipation in the two fluids, the analysis leading to the scalings in (2.6) could be extended to predict the wavelength selected during the coalescence or partial coalescence between two drops (Gilet *et al.* 2007), which would then provide us with the scaling of the diameter of the satellite drop produced (Zhang *et al.* 2015).

Figure 6 illustrates the way capillary waves excited during the rim retraction process deform the base of the cavity before the jet emerges. Indeed, the initially spherical cavity transforms into a shape that can be approximated by a truncated cone with an opening semiangle which hardly varies with *Oh*. However, the base of the truncated cone approximates the vertex as the Ohnesorge number increases. This

https://doi.org/10.1017/jfm.2019.161 Published online by Cambridge University Press

is due to the fact that the maximum amplitude of the nonlinear capillary waves is proportional to their wavelengths (Crapper 1957), with the wavelength increasing with Oh, as is clearly depicted in figure 5. In addition, figure 6 also shows that, when Oh equals a critical value, that from now on will be termed Oh_c, the amplitude of the selected wave is so large that its crest reaches the vertex of the cone. Therefore, for Ohnesorge numbers $Oh > Oh_c$, a bubble is entrapped below the collapsing cavity.

3. Scaling the jet speed

Our model starts by noticing that when the capillary wave that propagates down the surface of the collapsing bubble reaches the base of the truncated cone, it lowers the bottom of the gas cavity to a point closer to the vertex, as illustrated in figure 6. Since the amplitude of the wave at the base of the collapsing cavity is proportional to λ^*, and $\lambda^* \propto Oh^{1/2}$ for $Oh < Oh_c$, the distance between the crest of the wave, nearly the base of the cavity, and the vertex of the cone can be approximated as

$$\ell_{min} \propto 1 - (Oh/Oh_c)^{1/2}, \tag{3.1}$$

see figures 6 and 7. In addition, the shape of the cavity at the moment of jet eruption can be approximated by a cone of opening semiangle β and, therefore, the radius of the cavity can be expressed as

$$h(z) = z\tan(\beta). \tag{3.2}$$

Moreover, the balance between capillary pressure and liquid inertia at the cone interface yields (Zeff *et al.* 2000; Sierou & Lister 2004)

$$v_r \propto (\cos\beta)^{1/2} h^{-1/2}, \tag{3.3}$$

with v_r the radial component of the velocity field. Given the local radial velocity field (3.3) and making use of our ideas in Gekle *et al.* (2009) and Gekle & Gordillo (2010), we express the velocity field as the one created by a line of sinks of intensity

$$\mathrm{d}Q(z_0) = 2\pi h(z_0) v_r(z_0)\,\mathrm{d}z_0 \simeq 2\pi(\sin(\beta))^{1/2} z_0^{1/2}\,\mathrm{d}z_0, \tag{3.4}$$

where use of (3.3) has been made. Indeed, the local radial velocity field at the base of the cavity is created by a line of sinks with the intensity at the height z_0 calculated in (3.4) as the flow rate through a cylindrical surface of radius $h(z_0)$ and height $\mathrm{d}z_0$ at which the radial velocity is $v_r(z_0)$, see figure 7. The line of sinks with intensities given by (3.4) extends along the axis of symmetry a distance proportional to the length scale of the flow in the vicinity of the base of the cavity, namely, λ^*. The axial component of the velocity, v_z, at the vertical position z and the radial position ϵ can thus be expressed as

$$v_z = -\frac{\sqrt{\sin(\beta)}}{2}\int_{z_s}^{z_s+\lambda^*} \frac{z_0^{1/2}(z-z_0)}{[(z-z_0)^2+\epsilon^2]^{3/2}}\,\mathrm{d}z_0, \tag{3.5}$$

with $z_s = k\ell_{min}\cos\beta = kz_{min}$ the origin of the line of sinks and $k > 1$ a constant that determines where the line of sinks starts (see figure 7). The integration by parts of (3.5) for $\epsilon = 0$, yields

$$\int \frac{z_0^{1/2}\,\mathrm{d}z_0}{(z-z_0)^2} = \frac{1}{z^{1/2}}\int \frac{2x^2}{(1-x^2)^2}\,\mathrm{d}x = \frac{1}{z^{1/2}}\left(\frac{x}{1-x^2} - \ln\sqrt{\frac{1+x}{1-x}}\right), \tag{3.6}$$

https://doi.org/10.1017/jfm.2019.161 Published online by Cambridge University Press

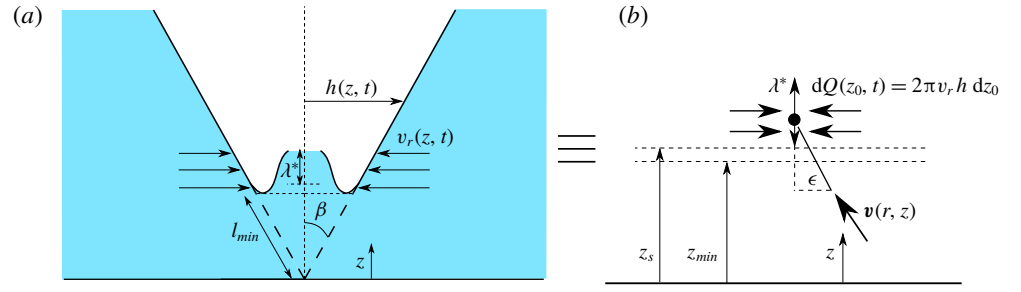


FIGURE 7. (Colour online) Panel (*a*) is a sketch representing the zoomed view of the cavity base in figure 6(*b*) for a value of the Ohnesorge number below the one for which bubbles begin to be entrapped. The base of the cavity at the moment the jet is about to be ejected can be approximated in this case by a truncated cone. The sketch does not represent the top part of the jet, which is about to be issued in figure 6(*b*). Panel (*b*) indicates that the velocity field can be approximated by a line of sinks with intensities $\mathrm{d}Q(z_0) = 2\pi h(z_0) v_r(z_0)\,\mathrm{d}z_0$ extending along the axis of symmetry a distance proportional to the wave amplitude, λ^*. The three horizontal lines in between the two images indicate that (*a*) is conceptually equivalent to (*b*) in what refers to the velocity field generated at the base of the cavity, which can be described using a continuous line of sinks.

with $z_0/z = x^2$. Since the velocity at a given location is mostly induced by nearby sinks, we can simplify this expression for $x \approx 1$. Hence,

$$\int \frac{z_0^{1/2}\,\mathrm{d}z_0}{(z-z_0)^2} \simeq \frac{1}{z^{1/2}}\frac{x}{1-x^2} = \frac{z_0^{1/2}}{z-z_0}. \tag{3.7}$$

Thus, the jet velocity at the axis of symmetry can be expressed as

$$v_{jet} \simeq v_z(z = z_{min}) = \frac{(kz_{min})^{1/2}}{(k-1)z_{min}} - \frac{(kz_{min}+\lambda^*)^{1/2}}{(k-1)z_{min}+\lambda^*}. \tag{3.8}$$

Two limits can be clearly distinguished in (3.8). If $\lambda^* \gg z_{min}$, which occurs only when the Ohnesorge number is such that $Oh \approx Oh_c$,

$$v_{jet} \propto z_{min}^{-1/2} \propto (1-(Oh/Oh_c)^{1/2})^{-1/2}. \tag{3.9}$$

If $\lambda^* \ll z_{min}$ namely, if $Oh \ll Oh_c$,

$$v_{jet} \propto Oh^{1/2}(1-(Oh/Oh_c)^{1/2})^{-3/2} \simeq KOh^{1/2}. \tag{3.10}$$

Interestingly, equation (3.9), which covers the regime in which the maximum jet velocity is attained, expresses that the jet velocity is proportional to the maximum velocity at the cavity walls, a fact indicating that the inertial mechanism governing the jet ejection process for $Oh \approx Oh_c$ is conceptually similar to the bazooka effect described in Birkhoff *et al.* (1948): indeed, the collapse of the conical cavity walls gives rise to the formation of the fast Worthington jet, in a manner similar that a fast thin metal jet is generated by the collapse of the conical walls of a metal-lined cavity.

The expressions for the jet velocity in (3.9)–(3.10) can only be valid while $Oh < Oh_c$. Indeed, for $Oh > Oh_c$, the crest of the waves will reach the vertex, the cavity will

https://doi.org/10.1017/jfm.2019.161 Published online by Cambridge University Press

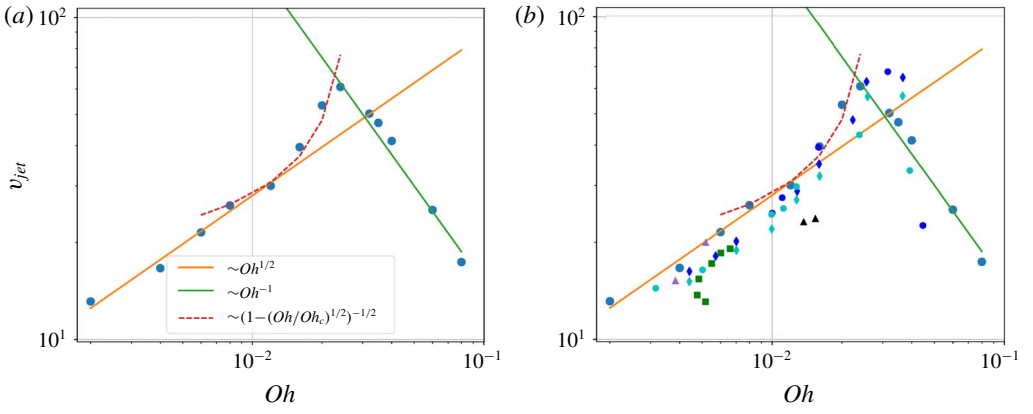


FIGURE 8. (Colour online) (*a*) Equations (3.9)–(3.10) and (3.12) predict the values of the jet velocity calculated numerically. The velocity increases with Oh until the crest of the wave reaches the vertex of the cone for $Oh = Oh_c$, see figure 6(*b*), and decreases for larger values of the Ohnesorge number. (*b*) Same figure as in (*a*), with large blue circles representing our numerical points, but showing also the data points of Deike *et al.* (2018) (blue and cyan small symbols, corresponding to $Bo = 10^{-3}$ and 10^{-2}, respectively), Ghabache *et al.* (2014) (green squares) and Krishnan *et al.* (2017) (purple triangles for water and black ones for glycerine–water with 48 % glycerine). From all these references, only points corresponding to $Bo < 0.05$ are shown.

adopt a purely conical shape and hence the velocity predicted by (3.9) would tend to infinity. Therefore, for $Oh > Oh_c$, the jet velocity is limited by viscous stresses and v_{jet} can be determined making use of the ideas in Riboux & Gordillo (2014), where the authors described the splash of droplets impacting a smooth dry substrate, where the case of splashing droplets is the two-dimensional analogue of the present physical situation. Riboux & Gordillo (2014) proposed a criterion that expresses that the jet will only be ejected at the instant when the deceleration caused to the emerging jet by viscous and capillary stresses is smaller than the deceleration experienced by the collapsing cavity walls. Applied to this particular physical situation, the criterion in Riboux & Gordillo (2014) yields

$$\rho \frac{V_{jet}^2}{R_{jet}} \propto \mu \frac{V_{jet}}{R_{jet}^2} \Rightarrow \frac{\rho V_{jet} R_{jet}}{\mu} \sim 1, \tag{3.11}$$

with R_{jet} the radius of the base of the cavity at the instant of jet ejection. In (3.11) we have taken into account that, in the present case, the collapse of the bubble is driven by capillarity (Zeff *et al.* 2000; Sierou & Lister 2004), namely, $\rho V_{jet}^2 \propto \sigma / R_{jet} \Rightarrow R_{jet} \propto \sigma / (\rho V_{jet}^2)$; inserting this result into (3.11) yields

$$V_{jet} \propto \frac{\sigma}{\mu} \Rightarrow v_{jet} = V_{jet} \left(\frac{\sigma}{\rho R} \right)^{-1/2} \propto Oh^{-1}. \tag{3.12}$$

The predictions for the jet velocity provided in (3.9)–(3.10) and (3.12) are confirmed in figure 8(*a*), where it can also be appreciated that the maximum jet velocity is reached for $Oh = Oh_c \simeq 0.02$, namely, for the value of the Ohnesorge number for

https://doi.org/10.1017/jfm.2019.161 Published online by Cambridge University Press

which the crest of the wave reaches the vertex of the cone, see figure 6(*b*). Equations (3.9)–(3.10), (3.12) as well as the results depicted in figures 6(*b*) and 8(*a*), reveal that the jet velocity decreases when a bubble is entrapped, a result which is identical to that found by Thoroddsen *et al.* (2018), who reported that the fastest Worthington jets produced by the collapse of the crater formed when a drop impacts a deep liquid pool, are those that bypass the pinch-off of a bubble. In addition, Thoroddsen *et al.* (2018) also reported that the radius of the gaseous dimple formed at the bottom of the crater approaches the axis of symmetry with a power law of the type τ^{γ}, with τ the time to singularity. The value $\gamma \sim 0.5$ reported in Thoroddsen *et al.* (2018) for the exponent of the power law describing the shrinking of the gas cavity, indicates that the velocity field around the gas thread is the one induced by a line of sinks located at the axis of symmetry (Gordillo 2008). All this evidence points to the fact that the physical model presented here can also be applied to describing the vertical jets commonly observed after a drop impacts on a deep pool of liquid.

Finally, note that the dependence of the jet velocity on viscosity expressed by (3.9)–(3.10) and (3.12), represented in figure 8(*b*), is in agreement with the numerical results in Deike *et al.* (2018) and is close to the experimental measurements reported in Ghabache *et al.* (2014) and Krishnan *et al.* (2017). Depending on the author, the experimental measurements show different values of v_{jet} for exactly the same values of the Bond and Ohnesorge numbers, so the deviations observed in figure 8(*b*) with experimental data can be attributed to slight asymmetries and also to the fact that the values reported in Ghabache *et al.* (2014) and Krishnan *et al.* (2017) refer to the velocity of the first drop ejected, which is smaller than the one reported here because of the capillary and viscous deceleration experienced by the jet tip before the drop is emitted. Indeed, note that our numerical values represented in figure 8(*b*) have been calculated at the instant of inception of the jet (see figure 1 and figure 3(f)). In addition, the small deviations appreciated in figure 8(*b*) between our results and those in Deike *et al.* (2018) can be attributed to the way the jet velocity is determined from the analysis of the numerical results: as pointed out above, here we report the initial jet velocity. Moreover, there exists another important difference between the results in Deike *et al.* (2018) and those reported here: the values of the Bond number are small but slightly different in both cases, and so are the initial shapes of the bubbles (Walls *et al.* 2015). Consequently, the tiny differences in Bo cause small differences in the initial static shape of the bubble and this fact influences the way the cavity deforms into a truncated cone, causing slight variations in the value of $Oh_c(Bo)$ for which a bubble is firstly entrapped. Indeed, for values of $Bo \leqslant 0.01$, Deike *et al.* (2018) found that $Oh_c \simeq 1000^{-1/2} \simeq 0.03$, a value which is slightly larger than the one corresponding to the case considered here, $Oh_c(Bo = 0.05) \simeq 0.02$. Since $Oh_c(Bo)$ decreases for increasing values of Bo, slightly smaller values of the Bond number, like the ones considered in Deike *et al.* (2018), cause the maximum jet velocity to be slightly displaced to larger values of the Ohnesorge number, as can be clearly appreciated in figure 8(*b*).

Figure 8(*b*) also shows that the jet velocity calculated using (1.1) follows the trend of the experimental measurements and of the numerical results in the limit $Oh \ll 1$, but fails to predict the observed trends for $Oh_c < Oh < Oh^*$, with $Oh^* \simeq 0.043$ the value in Gañán Calvo (2017). Indeed, figure 8(*b*) shows that, while the jet velocity decreases abruptly for $Oh_c < Oh < Oh^*$, the fit expressed by (1.1) predicts diverging jet velocities as $Oh \to Oh^*$. Hence, equation (1.1) happens to predict well a limited range of values of Oh, a fact that could explain why the numerical results in figure 3 in Lai *et al.* (2018) show a good collapse into an universal shape, but only for values of the Ohnesorge number in the range $Oh < 5000^{-1/2} \simeq 0.014 < Oh_c < Oh^* \simeq 0.04$.

https://doi.org/10.1017/jfm.2019.161 Published online by Cambridge University Press

The results depicted in figure 8(*b*) are also in qualitative agreement with Ghabache & Seon (2016) and Thoroddsen *et al.* (2018) where it is shown that, for increasing values of the Ohnesorge number, the jet velocity increases with Oh until the maximum jet velocity is reached for Oh_c and decreases for values of the Ohnesorge number larger than Oh_c. We cannot show a direct comparison with the results in Ghabache & Seon (2016) because the authors only reported the diameters of the drops ejected and, in the case of Thoroddsen *et al.* (2018), the authors analyse jets ejected after the impact of a drop on a free surface, the relationship between the impact Weber number and the shape of the cavity before it collapses not being fully clear.

4. Conclusions

When a hole is nucleated at the thin film that separates a bubble resting on a gas–liquid interface from the atmosphere, the subsequent retraction of the rim generates capillary waves of characteristic dimensionless wavelengths that increase with viscosity as $\lambda^* \propto Oh^{\alpha}$, with $\alpha = 1/2$ for $Oh \lesssim 0.02$ and $\alpha = 4/5$ for $Oh \gtrsim 0.02$. These waves propagate along the bubble interface towards the base of the collapsing cavity, which adopts the shape of a truncated cone. The vertical distance between the lower base of this cone and its vertex decreases linearly with λ^*. The radial flow field, which can be approximated by a line of sinks extending along the axis a distance proportional to λ^*, also induces vertical velocities that give birth to a fast and thin jet ejected upwards. The maximum jet velocity is attained for the value of the Ohnesorge number Oh_c for which the crest of the propagating wave reaches the vertex of the truncated cone. For $Oh \ll Oh_c$, $v_{jet} \propto Oh^{1/2}$, for $Oh \approx Oh_c$ the jet velocity is proportional to the maximum velocity of the collapsing cavity walls, $v_{jet} \propto (1 - (Oh/Oh_c)^{1/2})^{-1/2}$, this scaling being analogous to that found in lined cavities that make use of the bazooka effect (Birkhoff *et al.* 1948) and for $Oh > Oh_c$, $v_{jet} \propto Oh^{-1}$.

Let us point out that, in this contribution, we have only carried out numerical simulations for $Bo = 0.05$, a value which is sufficiently small to neglect the effect of gravity in the deceleration of the jet. However, the Bond number affects the initial shape of the bubble and hence, the opening semiangle of the cone and the value of Oh_c as well. Then, although not considered in this work, the effect of the Bond number on the jet ejection velocity can be straightforwardly rationalized using the theoretical framework presented here.

Acknowledgements

We wish to thank E. S. Quintero for providing us with the sketch in figure 7. This work has been supported by the Spanish MINECO under Projects DPI2014-59292-C3-1-P, DPI2014-59292-C3-2-P, DPI2017-88201-C3-1-R, DPI2017-88201-C3-3-R partly financed through European funds.

Supplementary movies

Supplementary movies are available at https://doi.org/10.1017/jfm.2019.161.

Appendix A

The expression for the viscous attenuation rate corresponding to the case $\delta \sim \lambda$ can be found from the kinetic energy balance

$$\frac{\mathrm{d}}{\mathrm{d}t}\int_{\Omega}\frac{\rho V^2}{2}\,\mathrm{d}\omega \sim \mu\int_{\Omega}\underline{\underline{\gamma}} : \underline{\underline{\gamma}}\,\mathrm{d}\omega, \tag{A 1}$$

https://doi.org/10.1017/jfm.2019.161 Published online by Cambridge University Press

with Ω the spatial region of characteristic volume $\sim R^3\lambda^2$ surrounding the wave and with

$$\underline{\underline{\gamma}} = \tfrac{1}{2}(\boldsymbol{\nabla V} + \boldsymbol{\nabla}^{\mathrm{T}}\boldsymbol{V}), \tag{A 2}$$

the deformation rate tensor. Notice that the zero shear stress condition at the interface requires that the velocity gradients within the boundary layer be of the order of the velocity gradients in the irrotational flow region, namely,

$$\boldsymbol{\nabla V} \sim \frac{V^*}{R\lambda}, \tag{A 3}$$

with V^* the characteristic velocity. Therefore, since in the case $\delta \sim \lambda$ most of the kinetic energy is dissipated within the boundary layer, of volume $\sim R^3\delta^2$, the balance of kinetic energy expressed by (A 1) yields

$$\frac{1}{T}\rho V^{*2}R^3\lambda^2 \sim \mu\frac{V^{*2}}{R^2\lambda^2}R^3\delta^2 \sim \mu\frac{V^{*2}}{R^2\lambda^2}\frac{\mu R}{\rho}\left(\frac{\rho R^3\lambda^3}{\sigma}\right)^{1/2} \Rightarrow \frac{1}{T} \sim \frac{\mu}{\rho R^2}Oh\lambda^{-5/2}, \tag{A 4}$$

where use of (2.2) has been made. It can be shown that the viscous dissipation rate corresponding to the irrotational flow limit in (2.3) can be recovered substituting δ^2 in (A 4) by λ^2.

REFERENCES

Batchelor, G. K. 1967 *An Introduction to Fluid Dynamics*. Cambridge University Press.

Bigg, K. E. & Leck, C. 2008 The composition of fragments of bubbles bursting at the ocean surface. *J. Geophys. Res.* **4113**, D11209.

Birkhoff, G., MacDougall, D. P., Pugh, E. M. & Taylor, S. G. 1948 Explosives with lined cavities. *J. Appl. Phys.* **19** (6), 563–582.

Crapper, G. D. 1957 An exact solution for progressive capillary waves of arbitrary amplitude. *J. Fluid Mech.* **2**, 532–540.

Deike, L., Ghabache, E., Liger-Belair, G., Das, A. K., Zaleski, S., Popinet, S. & Seon, T. 2018 Dynamics of jets produced by bursting bubbles. *Phys. Rev. Fluids* **3**, 013603.

Duchemin, L., Popinet, S., Josserand, C. & Zaleski, S. 2002 Jet formation in bubbles bursting at a free surface. *Phys. Fluids* **14**, 3000–3008.

Eggers, J. & Villermaux, E. 2008 Physics of liquid jets. *Rep. Prog. Phys.* **71** (3), 036601.

Gañán Calvo, A. M. 2017 Revision of bubble bursting: universal scaling laws of top jet drop size and speed. *Phys. Rev. Lett.* **119**, 204502.

Gañán Calvo, A. M. 2018 Scaling laws of top jet drop size and speed from bubble bursting including gravity and inviscid limit. *Phys. Rev. Fluids* **3**, 091601.

Gekle, S. & Gordillo, J. M. 2010 Generation and breakup of worthington jets after cavity collapse. Part 1. Jet formation. *J. Fluid Mech.* **663**, 293–330.

Gekle, S., Gordillo, J. M., van der Meer, D. & Lohse, D. 2009 High-speed jet formation after solid object impact. *Phys. Rev. Lett.* **102**, 034502.

Ghabache, E., Antkowiak, A., Josserand, C. & Seon, T. 2014 On the physics of fizziness: how bubble bursting controls droplets ejection. *Phys. Fluids* **26**, 121701.

Ghabache, E., Liger-Belair, G., Antkowiak, A. & Seon, T. 2016 Evaporation of droplets in a champagne wine aerosol. *Sci. Rep.* **6**, 25148.

Ghabache, E. & Seon, T. 2016 Size of the top jet drop produced by bubble bursting. *Phys. Rev. Fluids* **1**, 051901(R).

Gilet, T., Mulleners, K., Lecomte, J. P., Vandewalle, N. & Dorbolo, S. 2007 Critical parameters for the partial coalescence of a droplet. *Phys. Rev.* E **75**, 036303.

https://doi.org/10.1017/jfm.2019.161 Published online by Cambridge University Press

GORDILLO, J. M. 2008 Axisymmetric bubble collapse in a quiescent liquid pool. I. Theory and numerical simulations. *Phys. Fluids* **20** (11), 112103.

GORDILLO, J. M. & RODRÍGUEZ-RODRÍGUEZ, JAVIER 2018 Comment on revision of bubble bursting: universal scaling laws of top jet drop size and speed. *Phys. Rev. Lett.* **121**, 269401.

KRISHNAN, S., HOPFINGER, E. J. & PUTHENVEETTIL, B. A. 2017 On the scaling of jetting from bubble collapse at a liquid surface. *J. Fluid Mech.* **822**, 791–812.

LAI, C.-Y., EGGERS, J. & DEIKE, L. 2018 Bubble bursting: universal cavity and jet profiles. *Phys. Rev. Lett.* **121**, 144501.

DE LEEUW, G., ANDREAS, E. L., ANGUELOVA, M. D., FAIRALL, C. W., LEWIS, E. R., O'DOWD, C., SCHULZ, M. & SCHWARTZ, S. E. 2011 Production flux of sea spray aerosol. *Rev. Geophys.* **49**, 2010RG000349.

LHUISSIER, H. & VILLERMAUX, E. 2012 Bursting bubble aerosol. *J. Fluid Mech.* **696**, 5–44.

MACINTYRE, F. 1972 Flow patterns in breaking bubbles. *J. Geophys. Res.* **77**, 5211–5225.

MOORE, D. W. 1963 The boundary layer on a spherical gas bubble. *J. Fluid Mech.* **16**, 161–176.

POPINET, S. 2003 Gerris: a tree-based adaptive solver for the incompressible Euler equations in complex geometries. *J. Comput. Phys.* **190** (2), 572–600.

RIBOUX, G. & GORDILLO, J. M. 2014 Experiments of drops impacting a smooth solid surface: a model of the critical impact speed for drop splashing. *Phys. Rev. Lett.* **113**, 024507.

SIEROU, A. & LISTER, J. R. 2004 Self-similar recoil of inviscid drops. *Phys. Fluids* **16**, 1379–1394.

SONG, M. & TRYGGVASON, G. 1999 The formation of thick borders on an initially stationary fluid sheet. *Phys. Fluids* **11**, 2487–2493.

SPIEL, D. E. 1998 On the births of film drops from bubbles bursting on seawater surfaces. *J. Geophys. Res.* **103**, 907–918.

TAYLOR, G. I. 1959 The dynamics of thin sheets of fluid. III. Desintegration of fluid sheets. *Proc. R. Soc. Lond.* A **253**, 313–321.

THORODDSEN, S. T., TAKEHARA, K., NGUYEN, H. D. & ETOH, T. G. 2018 Singular jets during the collapse of drop-impact craters. *J. Fluid Mech.* **848**, R3.

VERON, F. 2015 Ocean spray. *Annu. Rev. Fluid Mech.* **47**, 507–538.

WALLS, P. L. L., BIRD, J. C. & BOUROUIBA, L. 2014 Moving with bubbles: a review of the interactions between bubbles and the microorganisms that surround them. *Integr. Compar. Biol.* **54**, 1014–1025.

WALLS, P. L. L., HENAUX, L. & BIRD, J. C. 2015 Jet drops from bursting bubbles: how gravity and viscosity couple to inhibit droplet production. *Phys. Rev.* E **92**, 021002(R).

WORTHINGTON, A. M. & COLE, R. S. 1896 Impact with a liquid surface, studies by the aid of instantaneous photography. *Phil. Trans. R. Soc. Lond* A **189**, 137–148.

ZEFF, B. W., KLEBER, B., FINEBERG, J. & LATHROP, D. P. 2000 Singularity dynamics in curvature collapse and jet eruption on a fluid surface. *Nature* **403**, 401–404.

ZHANG, F. H., THORAVAL, M.-J., THORODDSEN, S. T. & TABOREK, P. 2015 Partial coalescence from bubbles to drops. *J. Fluid Mech.* **782**, 209–239.

https://doi.org/10.1017/jfm.2019.161 Published online by Cambridge University Press